Nucleic Acids Research, 2025, **53**, gkaf435
https://doi.org/10.1093/nar/gkaf435
Gene regulation, Chromatin and Epigenetics

DNMT3A-dependent DNA methylation shapes the endothelial enhancer landscape

Stephanie Gehrs[1,2,3,*,†], Zuguang Gu[4,†], Joschka Hey[5], Dieter Weichenhan[5], Niklas Buckwalter[1,2], Moritz Jakab[1,2], Agnes Hotz-Wagenblatt[6], Kersten Breuer[5], Maria Llamazares Prada[5], Daniel Hübschmann[4,7,8,9], Katharina Schlereth[1,2], Christoph Plass[5,‡], Hellmut Augustin[1,2,*,‡]

[1]Division of Vascular Oncology and Metastasis, German Cancer Research Center (DKFZ), 69120 Heidelberg, Germany
[2]Department of Vascular Biology and Tumor Angiogenesis (CBTM), Medical Faculty Mannheim, Heidelberg University, 69120 Heidelberg, Germany
[3]Faculty of Biosciences, Heidelberg University, 69120 Heidelberg, Germany
[4]Computational Oncology Group, Molecular Precision Oncology Program, National Center for Tumor Diseases (NCT) Heidelberg and German Cancer Research Center (DKFZ), 69120 Heidelberg, Germany
[5]Division of Cancer Epigenomics, German Cancer Research Center (DKFZ), 69120 Heidelberg, Germany
[6]Core Facility Omics IT and Data Management (ODCF), German Cancer Research Center (DKFZ), 69120 Heidelberg, Germany
[7]Innovation and Service Unit for Bioinformatics and Precision Medicine (BPM), German Cancer Research Center (DKFZ), 69120 Heidelberg, Germany
[8]Pattern Recognition and Digital Medicine Group (PRDM), Heidelberg Institute for Stem Cell Technology and Experimental Medicine (HI-STEM) gGmbH, 69120 Heidelberg, Germany
[9]German Cancer Consortium (DKTK), 69120 Heidelberg, Germany

[*]To whom correspondence should be addressed. Email: s.gehrs@dkfz.de
Correspondence may also be addressed to Hellmut Augustin. Email: augustin@angioscience.de
[†]The first two authors should be regarded as Joint First Authors.
[‡]The last two authors should be regarded as Joint Last Authors.

Abstract

DNA methylation plays a fundamental role in regulating transcription during development and differentiation. However, its functional role in the regulation of endothelial cell (EC) transcription during state transition, meaning the switch from an angiogenic to a quiescent cell state, has not been systematically studied. Here, we report the longitudinal changes of the DNA methylome over the lifetime of the murine pulmonary vasculature. We identified prominent alterations in hyper- and hypomethylation during the transition from angiogenic to quiescent ECs. Once a quiescent state was established, DNA methylation marks remained stable throughout EC aging. These longitudinal differentially methylated regions correlated with endothelial gene expression and highlighted the recruitment of *de novo* DNA methyltransferase 3a (DNMT3A), evidenced by its motif enrichment at transcriptional start sites of genes with methylation-dependent expression patterns. Loss-of-function studies in mice revealed that the absence of DNMT3A-dependent DNA methylation led to the loss of active enhancers, resulting in mild transcriptional changes, likely due to loss of active enhancer integrity. These results underline the importance of DNA methylation as a key epigenetic mechanism of EC function during state transition. Furthermore, we show that DNMT3A-dependent DNA methylation appears to be involved in establishing the histone landscape required for accurate transcriptome regulation.

Graphical abstract

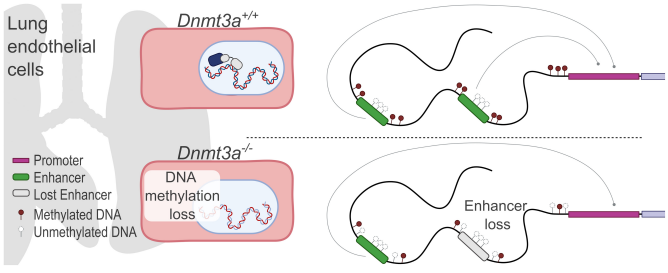

Received: November 21, 2024. **Revised:** March 28, 2025. **Editorial Decision:** April 26, 2025. **Accepted:** May 15, 2025

Introduction

Endothelial cells (ECs) acquire different cellular states during development and homeostasis via extrinsic environmental factors and intrinsic epigenetic mechanisms [1, 2]. While the vasculature expands during embryonic and postnatal development (referred to as the angiogenic state), it eventually transitions to a quiescent state in adulthood [3, 4]. This quiescent state is characterized by the cessation of cell proliferation and the secretion of paracrine and endocrine factors that support vascular maintenance [3]. Monitoring epigenetic and associated transcriptomic differences among these cellular states provides essential insight into the mechanisms governing cell state transition.

The epigenetic regulation of gene expression, mediated by DNA methylation, chromatin accessibility, and histone tail modifications, is tightly interconnected. It enables rapid and stable adaptation of cellular functions and responses to environmental cues [5, 6]. In mammals, DNA methylation occurs predominantly at CpG dinucleotides in ∼80% of the genome, except within CpG islands (CGIs). CGIs are short regions with a high frequency of CpG dinucleotides that are typically unmethylated and localized at regulatory elements [7]. Generally, DNA methylation is associated with gene silencing due to promoter methylation [8, 9]. Thus, DNA methylation inhibits the binding of the transcriptional machinery and therefore the initiation of gene expression.

Distal regulatory elements, such as enhancers, exhibit varying levels of DNA methylation [10] in a cell type-specific manner [11]. The identification of low-methylated enhancers, characterized by low CpG density [12], suggests that DNA methylation alone does not inherently lead to gene silencing. For example, CpG-poor regulatory regions often acquire low levels of DNA methylation upon transcription factor (TF) binding [12]. Furthermore, TFs have been shown to bind methylated CpG-poor regulatory regions, leading to their subsequent demethylation [13]. Conversely, DNA methylation can inhibit the binding of methylation-sensitive TFs by methylation of their binding motifs [14, 15]. In addition, methyl-CpG binding proteins, such as methyl-CpG binding protein 2 (MeCP2), methyl-CpG binding domain protein 1, and methyl-CpG binding domain protein 2 (MBD2), specifically recognize methylated CpG sites and act as transcriptional repressors of associated genes [16]. Notably, MeCP2 and MBD2 interact with histone deacetylases, linking DNA methylation-mediated transcriptional silencing to chromatin modification [17].

Examination of DNA methylation and chromatin accessibility in ECs isolated from different organs in infant mice revealed tissue-specific hypomethylated regions located in accessible areas distal to the transcription start site (TSS) [18]. Supporting a functional role of DNA methylation in gene regulation, tissue-specific differentially methylated regions (DMRs) were found in enhancers [19]. *In vivo*, the establishment of a homeostatic state in pulmonary ECs is accompanied by region-specific gain and loss of DNA methylation. Notably, the loss of DNA methylation at intragenic putative enhancers was suggested to induce homeostatic gene expression [4], in line with previous observations that DNA hypomethylation occurs at active enhancers [12, 20]. The importance of DNA methylation during development has been shown by individual and combined loss-of-function studies, which revealed embryonic or postnatal lethality in mice, particularly with the loss of DNA methyltransferases *Dnmt1*, *Dnmt3a*, and *Dnmt3b* [21, 22]. In the vasculature, the loss of *de novo DNA methyltransferase 3a* (*Dnmt3a*) resulted in DNA hypomethylation, which impaired EC proliferation and angiogenesis in the placental and retinal endothelium [23].

The observed functional roles of DNA methylation in the endothelium are well documented. However, the interplay of DNA methylation with other epigenetic layers, such as histone modifications and chromatin accessibility, and their interdependencies in the vasculature remains understudied. Here, we report the genome-wide *in vivo* endothelial methylome landscape, spanning the physiological development, quiescence, and aging of ECs. Our analysis revealed that major DNA methylation changes occur during the transition from an angiogenic state in infant mice to a quiescent state in adult mice. During further development and aging, DNA methylation patterns remain largely stable. We showed that DNMT3A is highly expressed in the pulmonary vasculature, and its loss resulted in reduced DNA methylation enriched in putative regulatory regions. These findings highlight DNMT3A's role in establishing DNA methylation in the pulmonary endothelium. Furthermore, comprehensive animal loss-of-function studies revealed that DNMT3A-dependent DNA methylation shapes angiogenic enhancers.

Materials and methods

Cell culture

HEK293T cells (Takara Bio Europe) were cultured in Iscove's Modified Dulbecco's Medium (IMDM) supplemented with 10% fetal calf serum (FCS) and 5% penicillin/streptomycin at 37°C and 5% CO_2. Human umbilical vein endothelial cells (HUVECs) (C-12253) were purchased from PromoCell and cultured in Endopan 3 supplemented with 3% FCS and supplements (PAN Biotech) at 37°C, 5% CO_2, and high humidity, maximum until passage 6. Cell culture plates were coated with 0.1% gelatin before cell seeding. For knockdown experiments upon lentiviral transduction with GIPZ-shRNA encoding virus [nsh: non-silencing verified negative control, RHS4346; *shDNMT3A#1*: small hairpin RNA (shRNA) against *DNMT3A*, V2LHS_202509; *shDNMT3A#2*: shRNA against *DNMT3A*, V3LHS_391162], cells were selected with puromycin (0.4 μg/mL) for 4–6 days.

Lentivirus production

HEK293T cells (Takara Bio Europe) were cultured in IMDM supplemented with 10% FCS and 5% penicillin/streptomycin at 37°C and 5% CO_2. For lentivirus production, 4×10^6 cells were seeded on 0.2% gelatin-coated 10-cm dishes in 8 mL medium. Transfection with a plasmid of interest needed for lentivirus production was performed using Lenti-X Packaging Single Shots (VSV-G) (Takara Bio Europe), which contained the transfection reagent and packaging plasmid, according to the manufacturer's instructions. The supernatant containing lentiviral particles was harvested on three consecutive days and filtered through a 0.22-μm filter to remove cellular debris. Lentiviral particles were purified with the Lenti-X Concentrator, and the resulting pellet was resuspended in 1/100th of the original input volume using phosphate-buffered saline (PBS). Fifty microliters of aliquots were stored at −80°C.

Lentiviral transduction

For lentiviral transduction, 1×10^5 cells were seeded in cell culture medium. After ~20 h, lentivirus was added for 16 h in 1 mL medium. For knockdown experiments upon lentiviral transduction with GIPZ-shRNA encoding virus, the following lentiviral constructs were used: nsh: non-silencing verified negative control, RHS4346; *shDNMT3A#1*: shRNA against *DNMT3A*, V2LHS_202509; and *shDNMT3A#2*: shRNA against *DNMT3A*, V3LHS_391162. Cells were washed once with PBS, and fresh medium was added 24 h before the antibiotic selection was started for 4–6 days.

Sprouting assay

Per spheroid, 400 HUVECs were suspended in 25 µL Dulbecco's modified Eagle medium (DMEM) containing 20% methylcellulose and seeded onto a plastic square plate. Fifty spheroids were used for one gel. Spheroids were allowed to form via the hanging-drop method at 37°C and 5% CO_2 for 24 h. Spheroids were harvested in PBS/5% FCS and centrifuged for 5 min at 150 × *g* without a break, and 500 µL methylcellulose/20% FCS was added to the spheroid pellet. For each gel, 62.5 µL Medium 199, 500 µL self-produced collagen, 6 µL of 2 M NaOH, and 50 µL of 1 M HEPES were prepared. The collagen solution was mixed with the spheroid/methylcellulose/20% FCS mixture and immediately transferred into a 24-well low-attachment cell culture plate. Gels were allowed to polymerize for 30 min at 37°C. After polymerization, 100 µL basal medium (without growth factor and FCS) or basal medium containing 100 ng human recombinant VEGF 165 (R&D, 293-VE) was added, and spheroids were incubated for 24 h at 37°C and 5% CO_2. Spheroids and developed sprouts were fixed in 4% Histofix (Roth) overnight. Per gel, pictures of ~10 spheroids were made using an Olympus IX71 microscope. The outgrowth of sprouts of each spheroid was measured with the Olympus image analysis software cellF. For each experimental condition, 10 gels were analyzed across three independent biological replicates.

Animal studies

C57BL/6N female mice were obtained from Janvier Labs. Heterozygous *B6 Dnmt3a* knockout (KO) mice were initially obtained from Jackson Laboratory (#018838) to generate homozygous *Dnmt3a* KO mice. Mice were bred at the dedicated animal facility barrier of the German Cancer Research Center under pathogen-free conditions. Mice were housed in individually ventilated cages in a temperature-controlled room with a 12-h light–dark cycle and free access to autoclaved food and water. Transgenic *B6 Dnmt3a* mice were obtained via in-house breeding. Pups were sacrificed at P7–8. All animal work was performed according to German national guidelines on animal welfare and the regulations of the regional council Karlsruhe under the following permit numbers: DKFZ370, G-82/19, and G-25/20.

Histology

To harvest murine lungs for immunofluorescence staining, the mice were euthanized with an overdose of anesthesia. The lung was inflated with undiluted O.C.T. compound (Sakura) until the lung volume matched the inner rib cage space. Subsequently, the trachea was clamped, and the inflated lung was dissected, immediately embedded, and frozen in O.C.T. compound.

For immunofluorescence staining, Tissue-Tek O.C.T.-embedded cryopreserved lung tissue was cut into 12 µm sections and fixed in zinc solution. Blocking and tissue permeabilization were performed in 10% normal donkey serum/3% bovine serum albumin, followed by incubation with the appropriate primary antibodies (anti-mouse CD31, BD Pharmingen, RRID: AB_396660, 1:100; anti-DNMT3A, Cell Signaling, #3598S, 1:100). After washing with tris-buffered saline with Tween 20 (TBST), the sections were incubated with the appropriate secondary antibodies. Hoechst 33258 was used for visualization of the nuclei. The slides were mounted using DAKO mounting medium, and images were taken with a Zeiss Axio Scan Z1 using an air 20×/0.8 Plan-APOCHROMAT objective.

Lung endothelial cell isolation by FACS

To FACS-sort pulmonary ECs, lung tissue was digested with 2% DNAseI (Roche, 20 mg/mL)/10% Liberase (Roche, dissolved in DMEM, high glucose to 2 mg/mL) in DMEM with high glucose (Gibco) for 15 min at 37°C. After the first incubation time, the tissue was gently disintegrated by passing the mixture through an 18-G needle, following a second incubation time of 15 min at 37°C. The single-cell suspensions were passed through a 100 µm cell strainer, and the enzymes were diluted with PBS/5% FCS. After centrifugation for 7 min at 4°C, erythrocyte lysis was performed by resuspending the cell pellet in ACK buffer following incubation for 5 min at room temperature. Lysis was stopped with PBS/5% FCS. A compensation control for single-antibody staining was used. The samples were incubated for 15 min at 4°C with an anti-mouse CD16/32 antibody (Purified Rat Anti-Mouse CD16/CD32, Clone 2.4G2 (RUO), BD Pharmingen, RRID: AB_394656, 1:100) to block nonspecific binding of immunoglobulin to Fc receptors. The cells were washed and incubated at 4°C for 20 min with CD31 mouse MicroBeads (Miltenyi Biotec) following LS column-based $CD31^+$ endothelial cell enrichment. The enriched cell suspensions were stained with an antibody mixture (Purified Rat Anti-Mouse CD31, Clone MEC 13.3 (RUO), BD Pharmingen, RRID: AB_396660, 1:100; FITC Rat Anti-Mouse TER-119/Erythroid Cells, BD Pharmingen, #561032, RRID: AB_396936, 1:200; Podoplanin Monoclonal Antibody [eBio8.1.1 (8.1.1)], Alexa Fluor 488, eBioscience, #53-5381-82, RRID: AB_1106990, 1:100; FITC Rat Anti-Mouse CD45, Clone 30-F11 (RUO), BD Pharmingen, #553080, RRID: AB_394609, 1:400; LYVE1 Monoclonal Antibody (ALY7), Alexa Fluor 488, eBioscience, #53-0443-82, RRID: AB_1633415, 1:250; and CD34 Monoclonal Antibody (RAM34), eFluor 450, eBioscience, #48-0341-82, RRID: AB_2043837, 1:50) at 4°C for 30 min before FACS. Dead cells were excluded by propidium iodide (Propidium Iodide Staining Solution, eBioscience, #00-6990-42, 1:20,000) staining. Live $CD45^-$/$TER119^-$/$LYVE1^-$/$PDPN^-$/ $CD31^+$/$CD34^+$ cells were sorted with a BD FACSAria ll (BD Biosciences).

RNA isolation

RNA from FACS-sorted ECs was isolated with an Arcturus PicoPure RNA Isolation Kit. The frozen pellet was resuspended in 50 µL of Arcturus PicoPure extraction buffer, and RNA was isolated according to the manufacturer's instructions. The RNA was eluted in 13 µL of RNase-free water, and the con-

centration was measured using a high-sensitivity RNA assay with a Qubit Fluorometer according to the manufacturer's instructions. The RNA was stored at −80°C.

Reverse transcription and quantitative measurement of RNA

Reverse transcription was performed using the QuantiTect Reverse Transcription Kit (Qiagen) according to the manufacturer's instructions. The obtained complementary DNA was diluted for real-time quantitative polymerase chain reaction (qPCR) analysis. TaqMan Fast Advanced Mastermix (Thermo Fisher Scientific) was used to detect differences in mRNA transcription levels. Reactions were performed in 384-well plates. Reactions, including water control, were performed in triplicate and run on a StepOnePlus Real-Time PCR System (Applied Biosystems). CT values were normalized to the respective CT values of the housekeeping gene (*Actb* for murine samples and *ACTB* for human samples), resulting in ΔCT values. Relative gene expression was assessed by normalizing the ΔCT values of individual samples to the average of the control ΔCT values, resulting in ΔΔCT values. The fold change was subsequently calculated by $2^{-\Delta\Delta CT}$. The TaqMan gene expression assays used were purchased from Thermo Fisher Scientific. The following TaqMan gene expression assays were used for murine samples: Mm00607939_S1 (*Actb*), Mm01151063_m1 (*Dnmt1*), Mm00432881_m1 (*Dnmt3a*), Mm01240113_m1 (*Dnmt3b*), Mm01169087_m1 (*Tet1*), Mm00524395_m1 (*Tet2*), Mm00805756_m1 (*Tet3*), and Mm00477872_m1 (*Uhrf1*). To assess the knockdown efficacy after lentiviral transduction of HUVECs, the following TaqMan gene expression assays were used for human samples: Hs01060665_g1 (*ACTB*) and Hs01027162_m1 (*DNMT3A*).

RNA sequencing

RNA sequencing libraries were prepared from FACS-sorted pulmonary ECs isolated from three mature adult mice (EC^{mAdu}) and three aged mice (EC^{aged}), as well as from three *Dnmt3a* wild-type (WT) and three *Dnmt3a* knockout (KO) pups. A sequencing library was generated with 10 ng of total RNA using the SMARTer Ultra Low RNA Kit for Illumina Sequencing (Clontech) according to the manufacturer's protocol. Sequencing reads (100 bp paired-end reads) were generated on the HiSeq2000 platform (Illumina).

Tagmentation-based whole-genome bisulfite sequencing

Tagmentation-based whole-genome bisulfite sequencing (T-WGBS) was performed as described [4]. WGBS libraries from mature adult mice (EC^{mAdu}) and aged mice (EC^{aged}) were generated using FACS-sorted pulmonary ECs, with three biological replicates for each age group. WGBS libraries were prepared from FACS-sorted pulmonary ECs isolated from three *Dnmt3a* WT and three *Dnmt3a* KO pups.

Assay for transposase accessible chromatin

Murine pulmonary ECs (5×10^4) were subjected to FACS, pelleted for 7 min at 500 × *g* in a prechilled (4°C) fixed-angle centrifuge, and resuspended in 50 μL of cold lysis buffer [10 mM Tris–HCl (pH 7.4), 10 mM NaCl, 3 mM $MgCl_2$, 0.1% NP-40, 0.1% Tween 20, 0.01% digitonin]. The nuclei isolation reaction was incubated for 3 min at room temperature. After lysis, 1 mL of ATAC-RSB [10 mM Tris–HCl (pH 7.4), 10 mM NaCl, and 3 mM $MgCl_2$] containing 0.1% Tween 20 was added and mixed. Nuclei were pelleted for 10 min at 500 × g at 4°C and resuspended in 50 μL of transposition buffer [10 mM Tris–HCl (pH 7.6), 5 mM $MgCl_2$, 10% dimethyl formamide, 2.5 μL transposase (100 nM final concentration), 0.1% Tween 20, 0.01% digitonin, 16.5 μL PBS, 5 μL H_2O]. Transposition reaction was incubated for 30 min at 37°C in a thermomixer shaking at 1000 rpm. The reaction was stopped with 20 μL of 5 M guanidinium thiocyanate, the ATAC (assay for transposase accessible chromatin) raw material was purified with a 2× volume of Ampure XP DNA purification beads, and the DNA was eluted in 25 μL of H_2O. The DNA eluate was PCR amplified using 1× NEBNext High Fidelity Mix in a total volume of 50 μL. The number of cycles used for library amplification depended on the observed amplification curve and varied between 10 and 15 cycles. ATAC libraries were purified with a 1.4× volume of Ampure XP DNA purification beads, and the DNA was eluted in 12 μL of elution buffer. Libraries were quality-controlled using the High Sensitivity DNA Bioanalyzer assay. ATAC experiments were conducted on FACS-sorted pulmonary ECs isolated from two litter-matched *Dnmt3a* WT and two *Dnmt3a* KO pups.

Antibody-guided chromatin tagmentation

Murine pulmonary ECs (1×10^5) were subjected to FACS, pelleted for 5 min at 300 × g at 4°C, and resuspended in 50 μL of cold complex formation buffer (1× CB) [50 mM Tris–HCl (pH 7.5), 150 mM NaCl, 0.05% Triton X-100, and 12.5% glycerol]. The cells were permeabilized for 10 min on ice. For each antibody, 0.16 μg of transposase (gifted from Dieter Weichenhan) was incubated with 3.3 μM adapter sequence in 1× CB buffer for 10 min. After adapter loading, 1 μg of antibody (H3K27ac, ab4729; H3K4me1, ab8895; H3K4me3, ab8580; H3K27me3, Cell Signaling, C36B11) was added, and the mixture was incubated for 30 min at room temperature. The transposon–adapter–antibody complex was added to the permeabilized cell suspension and incubated for 1 h at room temperature. In parallel, 7.5×10^2 permeabilized yeast nuclei were incubated with H2B (Hölzel diagnostika, BOS-M30930) targeting the transposase complex. After the 1 h incubation, the yeast–transposase–H2B antibody mixture was added to the murine cell suspension, which was subsequently washed three times with washing buffer [50 mM Tris–HCl (pH 7.5), 150 mM NaCl, and 0.05% Triton X-100]. The cell pellet was resuspended in 50 μL of washing buffer, and 1 μL of 1 M $MgCl_2$ was added to initiate the transposition reaction. The solution was incubated for 1 h at 37°C. The transposase reaction was stopped by adding 4 μL of 0.5 M ethylenediaminetetraacetic acid (pH 8), 2 μL of 10% sodium dodecyl sulfate, and 1 μL of proteinase K (20 mg/mL; Qiagen), and the mixture was incubated for 1 h at 55°C following DNA purification with a MinElute PCR Purification Kit (Qiagen). The DNA was eluted 2× with 12 μL of elution buffer. The DNA eluate was PCR amplified using 1× NEBNext High Fidelity Mix in a total volume of 50 μL. Antibody-guided chromatin tagmentation (ACT) libraries were purified with a 1.4× volume of Ampure XP DNA purification beads, and the DNA was eluted in 12 μL of elution buffer. Libraries were quality-controlled using the Agilent High Sensitivity D1000 ScreenTape System. ACT experiments were performed on FACS-sorted pulmonary ECs isolated from litter-matched *Dnmt3a* WT and *Dnmt3a*

KO pups. Three replicates per histone mark and per genotype were generated.

RNA-seq analysis

In this study, we generated new RNA-seq data for EC^{mAdu} and EC^{aged}, while publicly available transcriptome data for EC^{inf} and EC^{yAdu} were obtained from the Gene Expression Omnibus (GEO) under accession number GSE86600. The integration of both datasets allowed for a comprehensive analysis of expression dynamics across EC populations at different developmental stages. RNA-seq data for WT versus KO *Dnmt3a* ECs were generated as part of this study.

For all samples, low-quality bases were removed with the Fastq_quality_filter from the FASTX Toolkit (version 0.0.13) (https://github.com/agordon/fastx_toolkit) with 90% of the reads needing a quality Phred score >20. Homertools (version 4.7) [24] was used for polyA-tail trimming, and reads with a length <17 were removed. Filtered reads were quantified with Kallisto [25] using RefSeq transcripts of the mouse mm10 reference [26] (kallisto parameters -b 10 -t 3 –plaintext –single -l 292 -s 50). Later, in the customized analysis, the gene identifiers were converted to Ensembl IDs with the org.Mm.eg.db R package, and the Gencode vM4 annotation with only protein-coding genes was used for transcriptome annotation. TPM (Transcripts Per Million) was used as the normalization method. Differential expression analysis was performed with the DESeq2 package (version 1.38.3) [27]. Consensus clustering analysis was performed with the cola package (version 2.7.1) [28]. Functional enrichment analysis was performed with the clusterProfiler package (version 4.7.1) [29]. Gene Ontology (GO) term clustering and visualization were performed with the simplifyEnrichment package (version 1.9.4) [30]. Heatmap visualization was performed with the ComplexHeatmap package (version 2.15.4) [31] and EnrichedHeatmap (version 1.30.0) [32].

ATAC-seq analysis

ATAC-seq data for EC^{inf}, EC^{yAdu}, and EC^{mAdu} were obtained from the GEO under accession number GSE292008, while ATAC-seq data for WT versus KO *Dnmt3a* ECs were generated as part of this study.

ATAC-seq reads were processed using the ENCODE ATAC-seq pipeline kundajelab/atac_dnase_pipelines (version 1), unless otherwise specified [33]. As a reference, the mm10 genome was used. Reads were trimmed using Cutadapt and the parameters *-e 0.1 -m 5* and aligned using Bowtie2 allowing 0 multimapping and *-X2000 –mm –local* parameters. Duplicated reads were marked using Picard and mitochondrial reads were removed from the analysis.

Genomic annotations

Genes, exons, and introns were extracted from the Gencode vM4 annotation with only protein-coding genes. Promoters were extracted 2 kb upstream and 200 bp downstream of the TSS. CGIs were extracted from the UCSC table browser with the mm10 genome. CGI shores were extracted as 2 kb flanking regions of CGIs with no overlap with CGIs. SINE and LINE sequences were extracted from repeat masker tracks via the UCSC Table Browser.

Methylation analysis

In this study, we generated new DNA methylation data for EC^{mAdu} and EC^{aged}, while publicly available DNA methylation data for EC^{inf} and EC^{yAdu} were obtained from the GEO under accession number GSE87374. The integration of both datasets allowed for a comprehensive analysis of DNA methylation dynamics across EC populations at different developmental stages. WGBS data for WT versus KO *Dnmt3a* ECs were generated as part of this study.

WGBS samples were processed by our in-house standard pipeline. The raw reads were aligned with BWA mem (version 0.7.8) on the mouse genome mm10 and additionally concatenated with the lambda genome to infer the bisulfite conversion rate. Methylation data were processed in a unified way for all experiments. The raw methylation values (i.e. the fraction of reads that were methylated at each CpG position) for the CpG dinucleotides were merged into a single value by weighting the CpG coverage. The methylation values were subsequently smoothed with the bsseq package (version 1.34.0). A window-based method was used for detecting DMRs. The genome was split into 1 kb windows, and the mean methylation level was calculated for each window. Windows with fewer than five CpG sites were filtered out. This procedure converts the methylation data into a matrix; later, one-way ANOVA was performed to detect genomic windows that showed significant differences in methylation by adjusted P-value <0.01 and mean methylation differences >0.1. A window was annotated to a CGI if the overlap fraction was >50%. Association analysis between methylation and other genomic signals was performed with the EnrichedHeatmap package (version 1.28.1). For the correlation of DNA methylation with gene expression data, the correlated data were filtered by $|cor| > 0.5$ and adjusted P-value <0.05.

Motif analysis

Motif analysis was performed with HOMER (version 4.11.1) and the companion R package marge (version 0.0.4). Fold enrichment of a motif was calculated as the logarithm of the percentage of target sequence with motif and the percentage of background sequence with motif. A fold enrichment larger than zero represents the corresponding motif that exists more often in the target sequences than randomly distributed on the genome.

ACT-seq analysis

Trim Galore (version 0.4.4) [34] was applied in conjunction with Cutadapt (version 1.14) [35] using the non-default options "–nextera," "–paired," "–length_1 35," and "–length_2 35" to carry out quality and adapter trimming. Mapping of trimmed reads was performed against the Genome Reference Consortium Mouse Build version 38 by means of Bowtie2 (version 2.2.6) [36] using the "–very-sensitive" flag and an insertion length maximum of 2,500 bp. Mapped reads that belonged to the same lane-multiplexed library were combined using SAMtools merge (version 1.5) [37]. Discordant alignments with a Phred score <20 were removed using SAMtools view. Since Adey *et al.* [38] showed that fragments obtained from tagmentation cannot be <38 bp, all alignments that corresponded to fragment sizes below that threshold were removed. To represent the center of the transposition event, reads were shifted as previously described by Buenrostro *et al.* [39]. Furthermore, trimmed reads were aligned

against the *Saccharomyces cerevisiae* R64 reference genome, followed by post-alignment filtering. To obtain a library-specific scaling factor, we derived the multiplicative inverse of the number of filtered reads mapped against the yeast genome. Coverage tracks were made by means of the bamCoverage functionality of Deeptools (version 3.1.1) [40] using the non-default parameters "–ignoreForNormalization chrM chrY chrX" and "–effectiveGenomeSize 2652783500" as well as the "–scaleRatio" option to specify the spike-in-based scaling factor. The analysis procedure was implemented as fully containerized workflows using the common workflow language (version 1.0) [41], which is publicly accessible [42].

For the downstream analysis, peak calling was performed with Macs2 (version 2.1.2.1) [43]. For a specific histone mark with duplicates, we first obtained consensus peaks that occurred in at least two samples. Later, the genome was segmented by different combinations of histone marks. The chromatin states were assigned by the following rules: active promoters should only have H3K4me3 marks; optionally, H3K27ac and H3K4me1; bivalent promoters should have H3K4me3 and a repressed mark of H3K27me3; active enhancers should have H3K27ac or H3K4me1 marks; and bivalent enhancers should have H3K27ac or H3K4me1 with a repressor mark of H3K27me3.

Statistical analysis

All the statistical analyses were performed using GraphPad Prism Software version 8. The data are expressed as the mean ± standard deviation (SD). The performed statistical tests are specified in the figure legends. A *P*-value of <0.05 was considered to indicate statistical significance and is marked by asterisks ($*P<0.05$, $**P<0.01$, $***P<0.001$, **** $P<0.0001$). Unless otherwise stated, *n* represents the number of independent mice or samples in biological replicates analyzed per group or condition. The Benjamini–Hochberg (BH) method was used to control the false discovery rate in multiple hypothesis testing.

Results

DNA methylation changes occur during the angiogenic switch

Several studies have highlighted the role of DNA methylation in regulating gene expression, in which silencing of *cis*-regulatory elements (CREs) is accompanied by the establishment of DNA methylation [44, 45]. We consequently asked whether DNA methylation in ECs affects the silencing of regulatory elements during EC state transition from angiogenic to quiescent ECs.

To understand whether DNA methylation levels change upon longitudinal EC transition, we examined the genome-wide DNA methylation changes covering physiological time points of endothelial postnatal development, quiescence, and aging. ECs from an angiogenic endothelium in infants (EC^{inf}) to a quiescent endothelium in young and mature adult mice (EC^{yAdu} and EC^{mAdu}, respectively) and aged mice (EC^{aged}) were analyzed toward this end. The DNA methylation level in EC^{mAdu} and EC^{aged} was assessed by tagmentation-based WGBS, and publicly available DNA methylation data from EC^{inf} and EC^{yAdu}, generated with the same method, were re-analyzed [4] (Fig. 1A). Angiogenic ECs displayed distinctive changes in their DNA methylome compared to those of quiescent and aged states when all identified DMRs were considered (Fig. 1B). Notably, DNA methylation within CGIs, which are usually unmethylated and located in regulatory regions [7, 46], showed no clear difference between the developmental states (Fig. 1C). On the global level, angiogenic ECs gained DNA methylation upon transition into the quiescent state, and the methylome remained mostly stable during aging (Fig. 1D and Supplementary Fig. S1A). Over the longitudinal timeline, 1,558 DMRs were identified using EC^{inf} as a reference point, 79.85% of which were located distal to the TSS (TSS distance >5 kb) (Fig. 1D and Supplementary Fig. S1B, and Supplementary Table S1). These DMRs were designated as longitudinal DMRs (Fig. 1A). Classification of the identified longitudinal DMRs revealed minimal overlap with CGIs but a stronger association with CGI shores (regions adjacent to CGIs within a distance of 2 kb), which are known to correlate with tissue-specific gene expression [47]. To obtain detailed information about the genomic locations of the longitudinal DMRs, a genomic enrichment analysis was conducted, revealing an enrichment of hypomethylated longitudinal DMRs in genes and introns (Fig. 1E), whereas hypermethylated longitudinal DMRs were predominantly localized in CGI shores and CGIs (Fig. 1E).

The single-time point comparison between EC^{inf} and EC^{yAdu} resulted in the identification of 10,780 DMRs (Supplementary Fig. S1C and Supplementary Table S2). These cross-sectional DMRs were distal to the TSS and predominantly located in non-CGI-related regions (Supplementary Fig. S1C), consistent with observations for longitudinal DMRs. Together, the reanalysis of published DNA methylation data from infant and young adult mice supplemented with aging data confirmed the previously observed strong methylation difference during the transition from EC^{inf} to EC^{yAdu}. Even though angiogenic ECs were globally hypomethylated (Supplementary Fig. S1A), 67.52% of the longitudinal DMRs (1,052 DMRs) were consistently hypermethylated in the angiogenic state compared to all quiescent states (Supplementary Fig. S1D), indicating the involvement of active DNA methylation at these sites during angiogenesis.

Longitudinal DMRs correlate with endothelial gene expression

To understand the effect of longitudinal DMRs on gene expression, we correlated the DNA methylome with corresponding transcriptome data (Fig. 1A). In total, 448 continuous DMRs annotated to 315 unique genes (based on the nearest TSS) were identified ($|cor| > 0.5$ and adjusted *P*-values <0.05). These regions exhibited either a strong negative (meaning: loss of DNA methylation and gene upregulation or gain of DNA methylation and gene downregulation) or positive (meaning: loss of DNA methylation and gene downregulation or gain of DNA methylation and gene upregulation) transcriptomic correlation with the nearest genes ($|cor| > 0.5$; Fig. 1F and Supplementary Table S3).

Since DNA methylation is typically associated with gene silencing [8, 9], we referred to the association of longitudinal DMRs with negatively correlated gene transcription as "conventional" and the association with positively correlated gene transcription as "unconventional" (Supplementary Fig. S1E). In the context of endothelial growth and sustainability, key genes such as *Pecam1*, *Smad7*, and *Cav1* showed a conven-

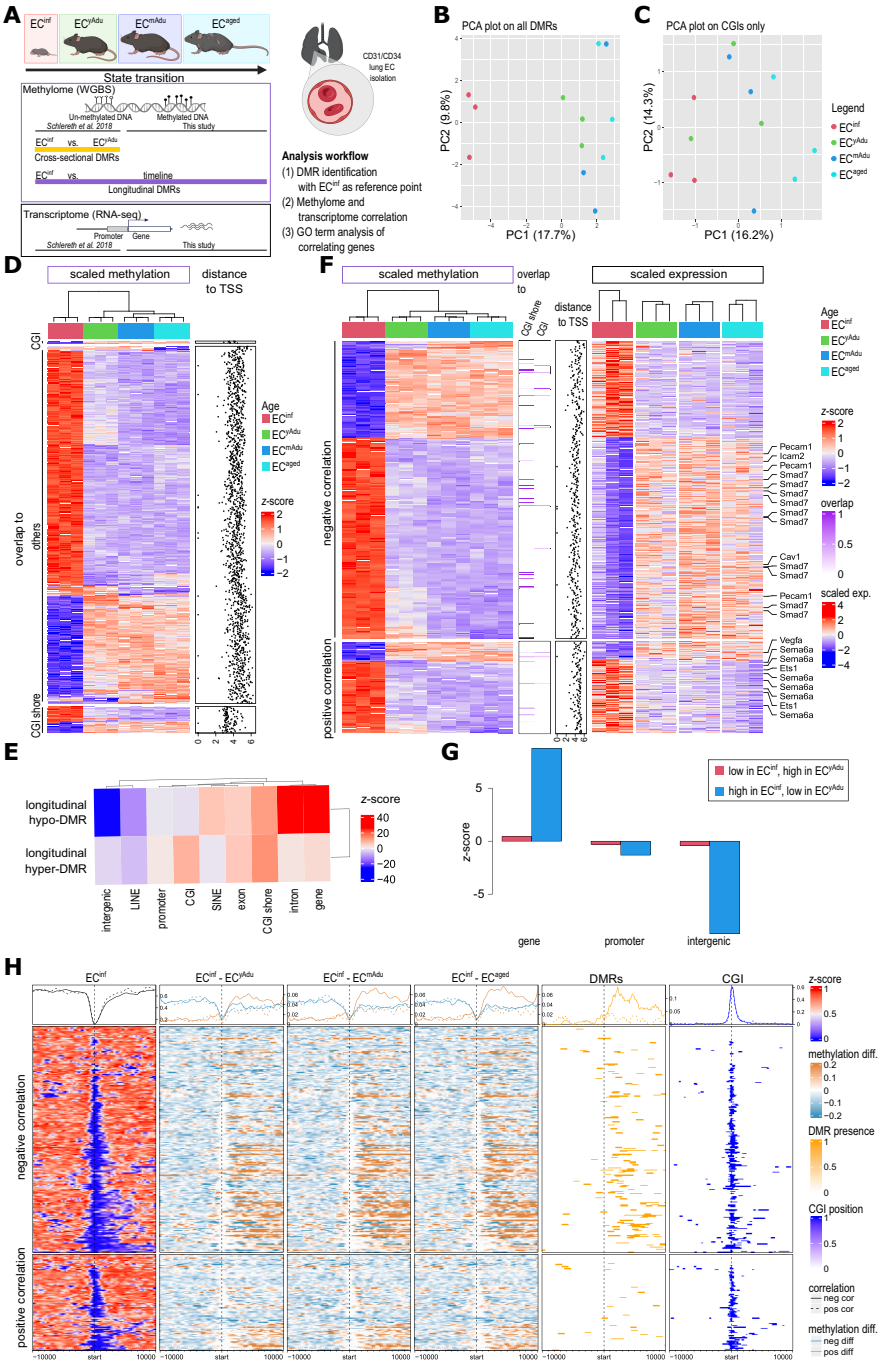

Figure 1. Methylation-correlating gene transcription shows differential DNA methylation distal to the TSS. (**A**) Scheme showing the longitudinal timeline for methylome sample collection and the additional methylome and transcriptome datasets used. For all the datasets, pulmonary capillary ECs were subjected to FACS and used for library generation. Single-datatype analysis and data integration were performed. In this study, methylome data were generated using WGSB. Identified DMRs between EC^{inf} and EC^{yAdu} were donated as cross-sectional DMRs. DMRs identified during EC state transition using EC^{inf} as a reference point were termed longitudinal DMRs. $n = 3$ for each age group. The scheme was created in BioRender. Augustin, H. (2025) https://BioRender.com/k83b042. (**B**) Methylome-based Principal Component Analysis (PCA) plot showing all the identified DMRs from all samples of the longitudinal timeline. (**C**) Methylome-based PCA plot showing DMRs detected in CGIs from all samples of the longitudinal timeline. (**D**) Heatmap displaying the scaled methylation level as *z*-score for 1,558 DMRs (left) and their distance to the nearest TSS (right). DMRs were clustered based on their genomic location (CGI shore, others, CGI). The distance to the nearest TSS is displayed as $\log_{10}()$. (**E**) Genomic enrichment analysis of longitudinal DMRs separated by their methylation direction into longitudinal hypo- and hyper-DMRs. EC^{inf} was used as a reference point. (**F**) Heatmap displaying the scaled methylation of 448 DMRs as *z*-score (left) with a high correlation ($|cor| > 0.5$ and adjusted *P*-values <0.05) to scaled gene expression (right). Endothelial genes showing a high correlation between DNA methylation and gene transcription are highlighted at the site of the gene expression heatmap (right). The middle plot shows the DMR association either as CGI or other, and the distance to the nearest TSS. (**G**) Bar plot showing the fold enrichment of positively correlated DMRs across genomic regions. Hypermethylated DMRs in EC^{yAdu} are labeled as "low in EC^{inf} and high in EC^{yAdu}", while hypermethylated DMRs in EC^{inf} are labeled as "high in EC^{inf} and low in EC^{yAdu}". (**H**) Heatmap enriched for the 315 genes showing a high correlation between methylation and gene expression ($|cor| > 0.5$ and adjusted *P*-values <0.05). Panel 1 displays the mean methylation level in a gene-centric way for angiogenic EC^{inf}, followed by panels 2–4, with the methylation difference between EC^{inf} and EC^{yAdu}, EC^{inf} and EC^{mAdu}, and EC^{inf} and EC^{aged} samples. Panel 5 shows the called DMRs. Panel 6 indicates the presence of a CGI at the TSS.

tional correlation, whereas *Ets1*, *Klf4*, *Sema6a*, and *Vegfa* exhibited an unconventional correlation (Fig. 1F).

Since increased DNA methylation is observed in the bodies of expressed genes [48], we investigated the genomic distribution of positively correlated DMRs. We categorized them toward this end into hypermethylated DMRs in EC^{inf} and hypermethylated DMRs in EC^{yAdu}. This analysis revealed that hypermethylated DMRs in EC^{inf} exhibited a strong over-enrichment within gene bodies, while simultaneously showing a strong under-enrichment in intergenic regions (Fig. 1G). Hypermethylated DMRs in EC^{yAdu} showed the same trend (Fig. 1G). These findings highlight the preferential localization of hypermethylated, positively correlated DMRs within gene bodies, supporting the established association between DNA methylation in gene bodies and active transcription. In line with this observation, increased DNA methylation in the angiogenic state was observed specifically downstream of the TSS of conventional methylation-to-expression associations (Fig. 1H).

To further assess the association of both negative and positive methylation-correlated gene transcription upon state transition, we performed GO analysis on the correlated genes, which revealed enrichment in biological processes such as development (vascular system development), cell migration, growth response, and cell adhesion (Supplementary Fig. S1F), indicating their potential role in angiogenesis. In summary, the TSS-downstream longitudinal DMRs predominantly exhibited a conventional correlation with the gene expression of the identified genes, associated with longitudinal DMRs that were involved mainly in vascular function.

Context-dependent DNA methylation regulates chromatin accessibility in endothelial CREs during state transition

To further analyze the impact of DNA methylation on the chromatin landscape, we integrated chromatin accessibility data generated by ATAC-seq. These data revealed that EC^{inf} showed higher accessibility at the TSS of genes with conventional methylation-to-expression associations compared to quiescent ECs (Fig. 2A). Notably, within these accessible regions, we observed enrichment of DNMT3A- but not DNMT3B-binding motifs [49] (Fig. 2A), suggesting the involvement of *de novo* methylation via DNMT3A during the EC state transition. This may result in DNA hypermethylation and subsequent gene suppression.

To understand how DNA methylation is established in the pulmonary endothelium, we analyzed the expression of DNA methylation modifiers. Compared to quiescent EC^{yAdu}, angiogenic EC^{inf} showed a significantly higher expression of *Dnmt3a*, which is involved in the establishment of DNA methylation (Fig. 2B). Furthermore, angiogenic EC^{inf} showed an upregulation of Ten-eleven translocation methylcytosine dioxygenase 1 (*Tet1*) (Fig. 2B), which removes DNA methylation. Notably, the co-expression of *Dnmt3a* and *Tet1* was shown to mediate the DNA methylation turnover at CGI shores [50]. The abundance of the *de novo* DNA methyltransferase DNMT3A was further confirmed by immunofluorescence staining of lung tissue samples, which revealed the nuclear localization of DNMT3A in lung sections obtained from EC^{inf} but not in those obtained from EC^{yAdu} tissue (Fig. 2C). Taken together, these data showed that DNA methylation in the angiogenic state is associated with chromatin accessibility in CREs, which in turn might contribute to changes in gene expression upon transition into quiescence. Furthermore, these data suggest that DNMT3A functions in shaping the epigenetic landscape during EC state transition.

DNMT3A fine-tunes gene expression via methylation at the periphery of the CGI

Given that angiogenic EC^{inf} highly expressed *Dnmt3a* (Fig. 2B and C), we hypothesized that DNA methylation changes may instruct gene expression during the EC state transition in the lung. To further assess the relevance of DNMT3A-introduced DNA methylation, we profiled FACS-sorted pulmonary capillary ECs isolated from infant $Dnmt3a^{KO}$ (referred to as KO) and $Dnmt3a^{WT}$ (referred to as WT) infants (Fig. 3A). Compared to WT, KO ECs exhibited a global loss of DNA methylation (Supplementary Fig. S2A). Almost all DMRs were hypomethylated (>99.9%) in the KO endothelium (Supplementary Fig. S2B and Supplementary Table S4). Hereafter, these DMRs were denoted as DNMT3A-dependent DMRs.

We examined the distance of DMRs to the nearest TSS as well as their genomic location. Out of all DNMT3A-dependent DMRs, 83.74% (38,949 DMRs) were located distal to their nearest TSS (TSS distance > 5 kb) (Fig. 3B) and showed a strong enrichment for CGI shores (0.54 $\log_2$-fold change enrichment), genes (0.54 $\log_2$-fold change enrichment), and intron regions (0.56 $\log_2$-fold change enrichment) (Fig. 3C). Local DMRs (TSS distance $\leq$ 5 kb) exhibited the strongest enrichment in CGI shores (4.15 $\log_2$-fold change enrichment) and promoters (3.76 $\log_2$-fold change enrichment) (Fig. 3D). The enrichment of DNMT3A-dependent DMRs in promoters and CGI shores pointed toward their functional role in gene regulation. Accordingly, we hypothesized that the loss of *Dnmt3a* and therefore DNA methylation would lead to gene deregulation. Strikingly, compared with WT controls, KO ECs showed only 413 (adjusted *P*-value <0.05) DEGs (Supplementary Fig. S2C and Supplementary Table S5), and 62.5% (258 genes) of the DEGs were associated with DNA methylation loss (Fig. 3E), among which were proangiogenic genes such as *Aplnr*, *Nrp1*, and *Fli1*. GO analysis of these genes revealed enrichment in the biological functions of development, morphogenesis, and signal response (Fig. 3F).

To investigate the role of DNMT3A in angiogenesis, we evaluated the angiogenic potential of HUVECs using a gel-embedded sprouting assay (Fig. 3G), a well-established *in vitro* surrogate of angiogenesis. Prior to conducting the sprouting assay, *DNMT3A* knockdown was induced using shRNAs. Efficient knockdown was achieved with two independent shRNAs targeting *DNMT3A* (*shDNMT3A#1* and *shDNMT3A#2*), reducing *DNMT3A* transcript levels to ~30% compared to a control shRNA (*nsh*) (Fig. 3H). In spheroid assays, *DNMT3A* knockdown reduced the number of vascular sprouts in response to rhVEGF supplementation, which was used to induce angiogenic sprouting (Fig. 3I and J). Notably, a significant reduction in average sprout length was observed only in response to rhVEGF in the *shDNMT3A#2* cell line (Fig. 3K), likely due to the stronger knockdown efficiency of this shRNA (Fig. 3H). This observation was in line with our previous finding that loss of DNA methylation impairs the angiogenic capacity of ECs [23]. Taken together, these data showed that DNMT3A-dependent DNA methyla-

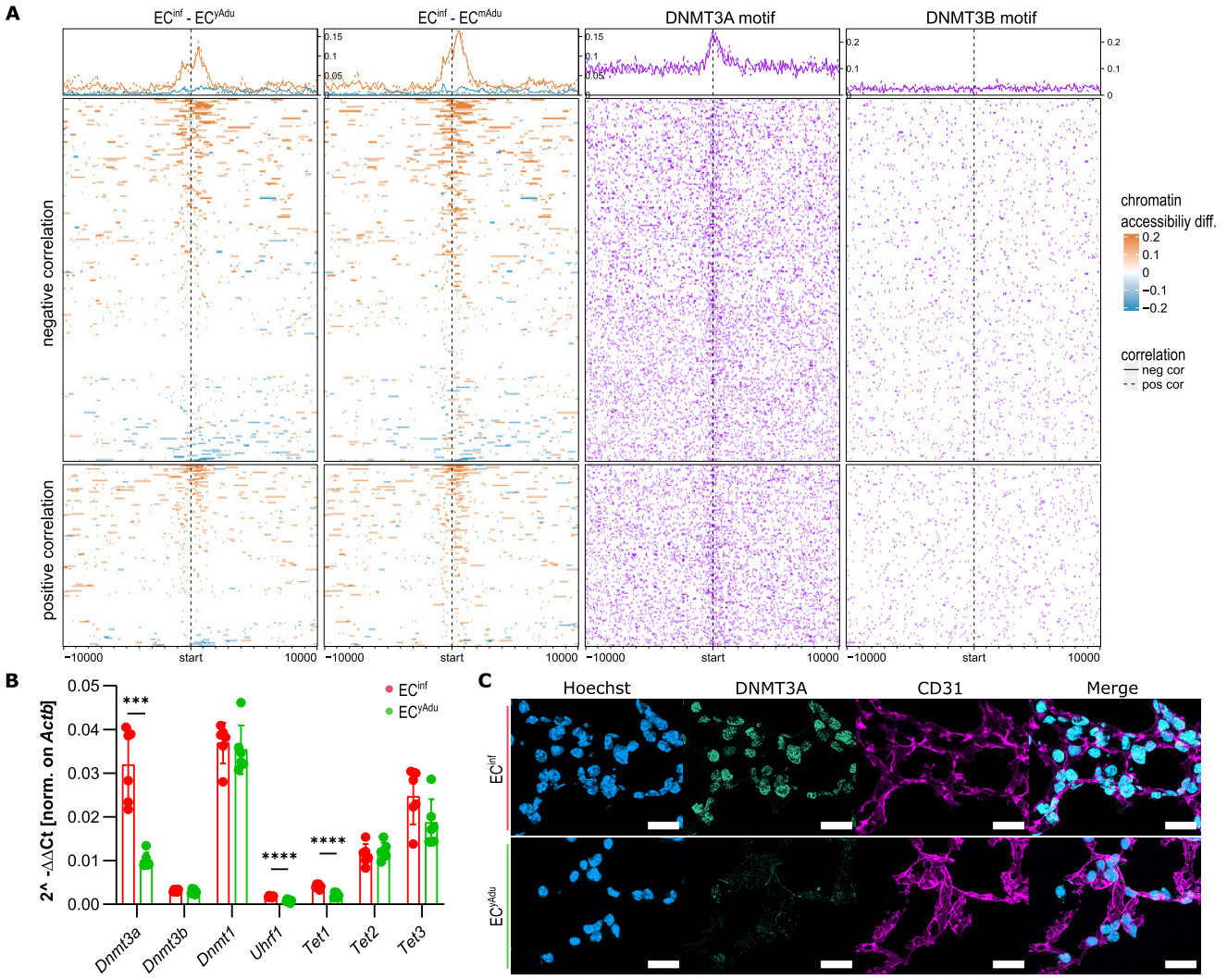

Figure 2. Context-dependent impact of DNA methylation on chromatin accessibility. (**A**) Differential chromatin accessibility in the TSS of genes showing a methylation–transcription correlation in EC^{inf} versus EC^{yAdu} (panel 1) and in EC^{inf} versus EC^{mAdu} (panel 2). The enrichment plot displays the binding motives for DNMT3A (panel 3) and DNMT3B (panel 4). $n = 3$ for each age group. (**B**) qPCR of pulmonary ECs isolated from infant and young adult mice showing the expression of DNA modifiers. $n = 6$ per age group. The data are presented as the means ± SDs. *P*-values were determined by the Mann–Whitney test. ***$P < 0.001$, **** $P < 0.0001$. (**C**) Representative images of infant and young adult lung sections stained for CD31 (vascular surface), DNMT3A (DNA methyltransferase), and Hoechst (nucleus). Scale bar: 20 μm.

tion is found mainly in putative CREs and affects the expression of a subset of endothelial genes involved in development.

DNMT3A maintains endothelial CRE composition

As DNMT3A-dependent DMRs were significantly enriched in putative CREs (Fig. 3C and D), we further investigated the impact of DNA methylation loss on regulatory elements via ATAC-seq of angiogenic *Dnmt3a* WT and KO ECs (Fig. 3A). Overall, the loss of *Dnmt3a* resulted in reduced chromatin accessibility, with the major loss observed in distal accessible regions (Supplementary Fig. S2D and Supplementary Table S6). In particular, we observed reduced enrichment of chromatin accessibility in CGIs but not in promoter regions (Supplementary Fig. S2E), suggesting changes in CREs and potential enhancers.

Due to the inherent difficulties in correctly relating distal CREs to genes (enhancer elements can bypass their closest gene promoter), we first analyzed local chromatin accessibility changes and their effects on gene expression. We identified 12,474 open chromatin regions at a gene TSS that were shared between *Dnmt3a* WT and KO ECs (Supplementary Fig. S2F). As expected, the associated genes were not differentially expressed (Supplementary Fig. S2F). Analysis of accessible regions that were unique to each genotype resulted in 454 unique accessible TSS in *Dnmt3a* WT ECs (Supplementary Fig. S2G) and 44 unique accessible TSS in *Dnmt3a* KO ECs (Supplementary Fig. S2H). For both scenarios, no significant changes in gene expression were observed. Additionally, GO term analysis revealed similar enrichment of biological processes for both shared and unique accessible regions (Supplementary Fig. S2I). These data indicate that the loss of DNA methylation in the *Dnmt3a* KO endothelium resulted in reduced chromatin accessibility of primarily distal CREs. Furthermore, the rare changes in the accessibility of promoter regions close to a gene TSS did not result in gene expression changes.

To further determine whether the distal regions affected by the loss of DNA methylation are endothelial enhancers,

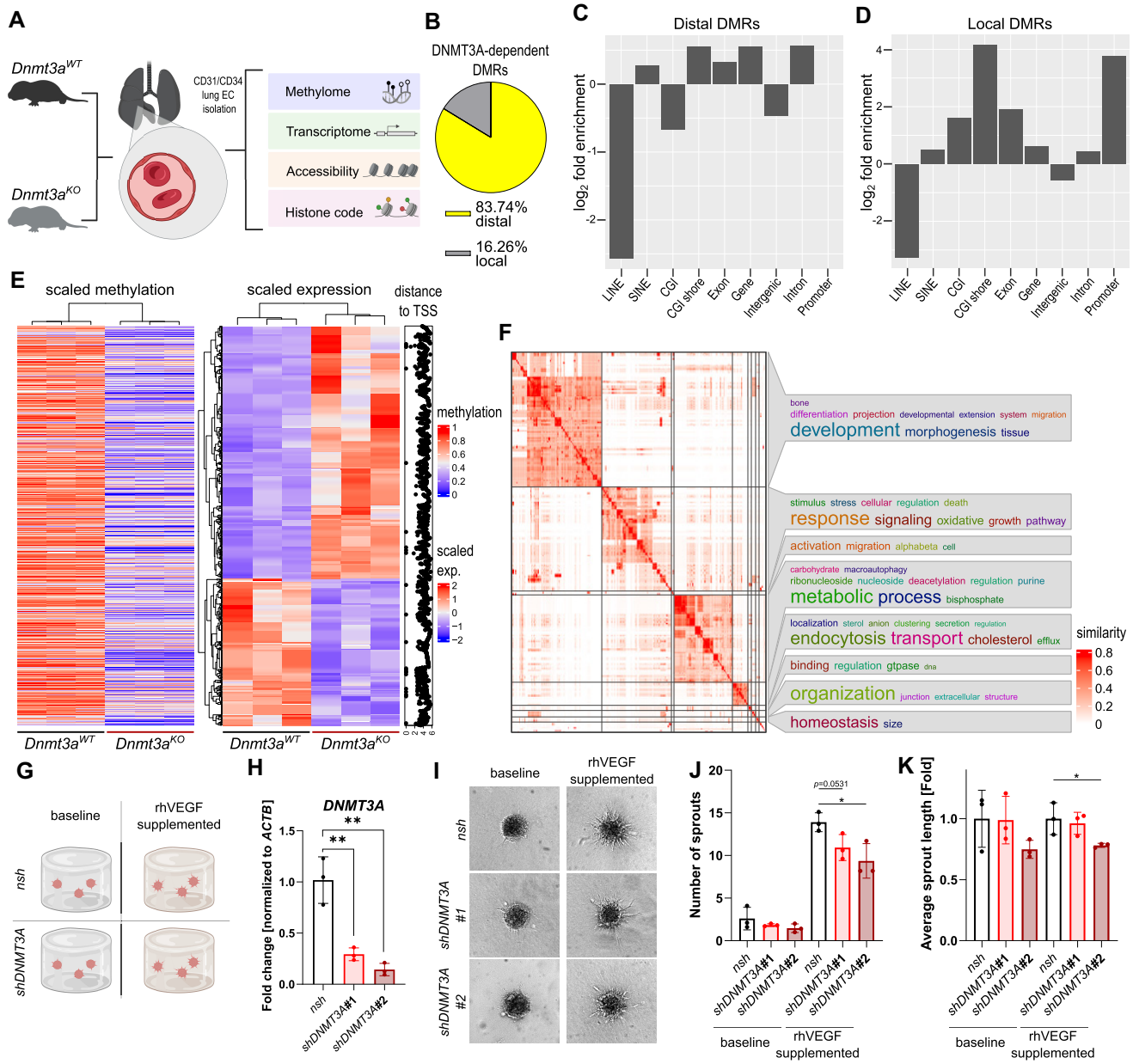

Figure 3. Loss of DNMT3A-dependent DNA methylation results in mild gene deregulation. (**A**) Schematic overview showing the sample collection of pulmonary ECs isolated from *Dnmt3a* WT and *Dnmt3a* KO infant mice. FACS-sorted pulmonary ECs were further used for methylome, transcriptome, chromatin accessibility, and histone landscape analysis. The scheme was created in BioRender. Augustin, H. (2025) https://BioRender.com/k83b042. (**B**) Pie diagram displaying the relative number of DMRs upon the loss of *Dnmt3a* located distal (distance > 5 kb) or local (distance ≤ 5 kb) to the nearest TSS. (**C**) Genomic enrichment of distal DNMT3A-dependent DMRs. (**D**) Genomic enrichment of local DNMT3A-dependent DMRs. (**E**) Heatmap showing DNMT3A-dependent DMRs (left) and 258 associated genes (middle) that were differentially expressed (adjusted *P*-value <0.05) in *Dnmt3a* KO ECs compared to WT ECs. The distance of the DMRs to the gene TSS is shown on the right as $\log_{10}()$ in bp. For both, methylome and transcriptome analyses, three biological replicates were used for each genotype. (**F**) Gene ontology analysis based on the biological functions of 258 differentially expressed genes (DEGs) that were associated with DNMT3A-dependent DNA methylation changes. A heatmap (left) displays the clustering of GO terms based on similarity (range: 0–0.8). The letter size represents the significance of the GO term (right). (**G**) Schematic representation of the sprouting assay. Control and shDNMT3A cell lines were analyzed under baseline conditions and angiogenic stimulation with recombinant human VEGF (rhVEGF) supplementation. The scheme was created in BioRender. Augustin, H. (2025) https://BioRender.com/k83b042. (**H**) Quantification of *DNMT3A* knockdown efficacy in HUVECs following lentiviral transduction with *shDNMT3A* (sh#1, sh#2) or control shRNA (*nsh*). Data represent $n = 3$ biological replicates per cell line and are presented as mean ± SD. Statistical significance was assessed using an unpaired *t*-test. ***P* <0.01. (**I**) Representative images of spheroids formed by HUVECs transduced with control shRNA or *shDNMT3A*. The spheroid assay was conducted under baseline conditions or upon angiogenic induction with rhVEGF. (**J**) Quantification of the number of sprouts in spheroids formed by HUVECs transduced with control shRNA or *shDNMT3A* constructs. Data represent $n = 3$ biological replicates per cell line and are presented as the mean ± SD. Statistical significance was determined using an unpaired *t*-test. **P* <0.05. (**J**) Quantification of the average sprout length, expressed as fold change, in HUVECs transduced with control shRNA or *shDNMT3A* constructs. Data represent $n = 3$ biological replicates per cell line and are presented as the mean ± SD. Statistical significance was determined using an unpaired *t*-test. **P* <0.05.

we performed extensive characterization of the histone landscape using ACT-seq (Supplementary Fig. S3A). We mapped the genome-wide distribution of histone tail modifications, such as H3K4me1, H3K4me3, H3K27ac, and H3K27me3. Notably, the combinatorial intersection of histone marks was used to molecularly characterize promoters (H3K4me3, H3K27ac) and enhancers (H3K4me1, H3K27ac) and determine their potential in gene regulation (Supplementary Fig. S3B). This integration strategy enabled the identification of active, bivalent, and poised enhancers, as well as active, bivalent, and silent promoters, and repressed regions (Supplementary Fig. S3B).

In accordance with the expected genomic localization patterns, promoters were localized near the TSS, whereas enhancers were found at greater distances from the TSS (Supplementary Fig. S3C and D). Furthermore, the detected peaks for the sampled histone marks were enriched for regions with gene regulatory functions (Supplementary Fig. S3E). To explore how DNA methylation could affect active promoters and enhancers in angiogenic ECs, we integrated the corresponding DNA methylation data. In general, promoters were found at DNA methylation-free CGIs and with accessible chromatin in both WT and *Dnmt3a* KO ECs (Supplementary Fig. S4A and B). KO ECs showed a broader unmethylated region in the periphery of the identified promoters (Supplementary Fig. S4B). The associated gene expression in both WT and KO ECs was not changed. To systematically assess the effect of enhancer changes in *Dnmt3a* KO ECs on gene expression, active enhancer regions identified in WT and KO ECs were centered around a TSS, resulting in 1,187 active enhancer regions for *Dnmt3a* WT and 444 active enhancer regions for KO ECs (panel 1 in Supplementary Fig. S5A and B). The reduction of active enhancers to only the ones that are centered around a TSS allowed us to associate these enhancers with gene expression data. The identified enhancers (centered around a TSS for gene expression association) exhibited less prominent colocalization with CGIs in *Dnmt3a* KO ECs, but showed as promoters accessible chromatin and DNA hypomethylation in their core regions (Supplementary Fig. S5A and B). Upon *Dnmt3a* loss, we observed an expansion of the unmethylated enhancer periphery in line with the detected enrichment of DMRs in CGI shores (Fig. 3C and D), suggesting that DNMT3A-dependent DNA methylation is more relevant at the flanking regions of these elements rather than their central functional sites.

Furthermore, our analysis revealed substantial changes in regulatory element distribution upon *Dnmt3a* loss (Fig. 4A, summarized in Supplementary Table S7). A detailed breakdown of WT-specific CREs is provided in Supplementary Table S8, and KO-specific CREs are listed in Supplementary Table S9. Specifically, the number of active promoters increased from 7,482 in WT ECs to 10,954 in KO ECs, suggesting a gain in promoter activity. This change has previously been observed in mouse embryonic stem cells lacking *Dnmt3a*, where the loss of DNA methylation led to increased H3K4me3 deposition [51]. Similar findings have been reported upon *Dnmt1* deletion, further supporting the role of DNA methylation being indirectly involved in histone mark deposition [20]. Similarly, bivalent promoters increased from 6,044 to 8,299, indicating that *Dnmt3a* loss may promote the establishment of bivalent chromatin states at previously inactive loci.

Conversely, we observed a notable reduction in active enhancers, decreasing from 79,083 in WT ECs to 41,699 in KO ECs. This striking loss of active enhancers highlighted DNMT3A's role in maintaining enhancer activity and suggested that DNA methylation may be critical for enhancer stability. Additionally, bivalent enhancers were reduced by >50% (from 2,286 in WT to 1,087 in KO ECs), further emphasizing a shift in the enhancer landscape.

The number of poised enhancers remained largely unchanged (899 in WT versus 882 in KO ECs), indicating that these elements were relatively unaffected by DNMT3A depletion. In contrast, silent promoters increased from 1,648 in WT ECs to 2,106 in KO ECs. Finally, the number of repressed regions nearly doubled, rising from 9,433 in WT ECs to 18,167 in KO ECs, indicating a widespread shift toward a repressive chromatin state. This increase in repressive elements, combined with the loss of active enhancers, suggested that DNMT3A-dependent DNA methylation plays a crucial role in maintaining an open chromatin environment at regulatory regions. Overall, these findings demonstrate that DNMT3A loss leads to widespread enhancer depletion and an increase in repressive chromatin states, with potential consequences for gene regulation in ECs.

Chromatin state reprogramming in *Dnmt3a*-deficient ECs

To investigate the chromatin state transitions following *Dnmt3a* loss, we quantified the redistribution of CREs. The total genomic coverage (in bp) of each CRE category was toward this end quantified in *Dnmt3a* WT ECs and tracked to their corresponding states in KO ECs. If a region was annotated to one of the previously identified CRE categories (Supplementary Fig. S3B) in one genotype but lacked an annotation in the other, it was classified as "others" (displayed in gray in the circos plots). This analysis allowed us to determine how individual regulatory elements changed classification upon *Dnmt3a* loss, which CREs retained their identity versus those that transitioned into new regulatory states, and the proportion of regions that lost clear CRE classification ("others"). Subsequent findings revealed widespread chromatin remodeling (Supplementary Table S10) with notable shifts from active enhancers in WT ECs to non-assigned chromatin states (referred to as "others") in *Dnmt3a* KO ECs (Fig. 4B and C).

In detail, active enhancers in both WT and KO ECs exhibited the largest genomic coverage (23,267,740 bp in WT ECs (Fig. 4C) and 18,026,290 bp in KO ECs), but following *Dnmt3a* loss, a substantial fraction transitioned into different regulatory states. In total, 37.63% (8,755,899 bp) of active enhancers identified in WT ECs retained their active enhancer identity in KO ECs. A minor fraction transitioned into bivalent enhancers (1.09% corresponding to 253,737 bp), poised enhancers (0.38% corresponding to 89,126 bp), repressed regions (0.30% corresponding to 70,492 bp), and silent promoters (0.04% corresponding to 10,155 bp). Notably, 12,949,262 bp (55.65%) of formerly active enhancers were reassigned as "others", suggesting a substantial loss of enhancer identity upon *Dnmt3a* KO (Fig. 4C and Supplementary Table S10).

Active promoters in WT ECs (4,709,225 bp total genomic coverage) were largely preserved in KO ECs (59.46% corresponding to 2,800,263 bp), whereas 799,567 bp (16.98%)

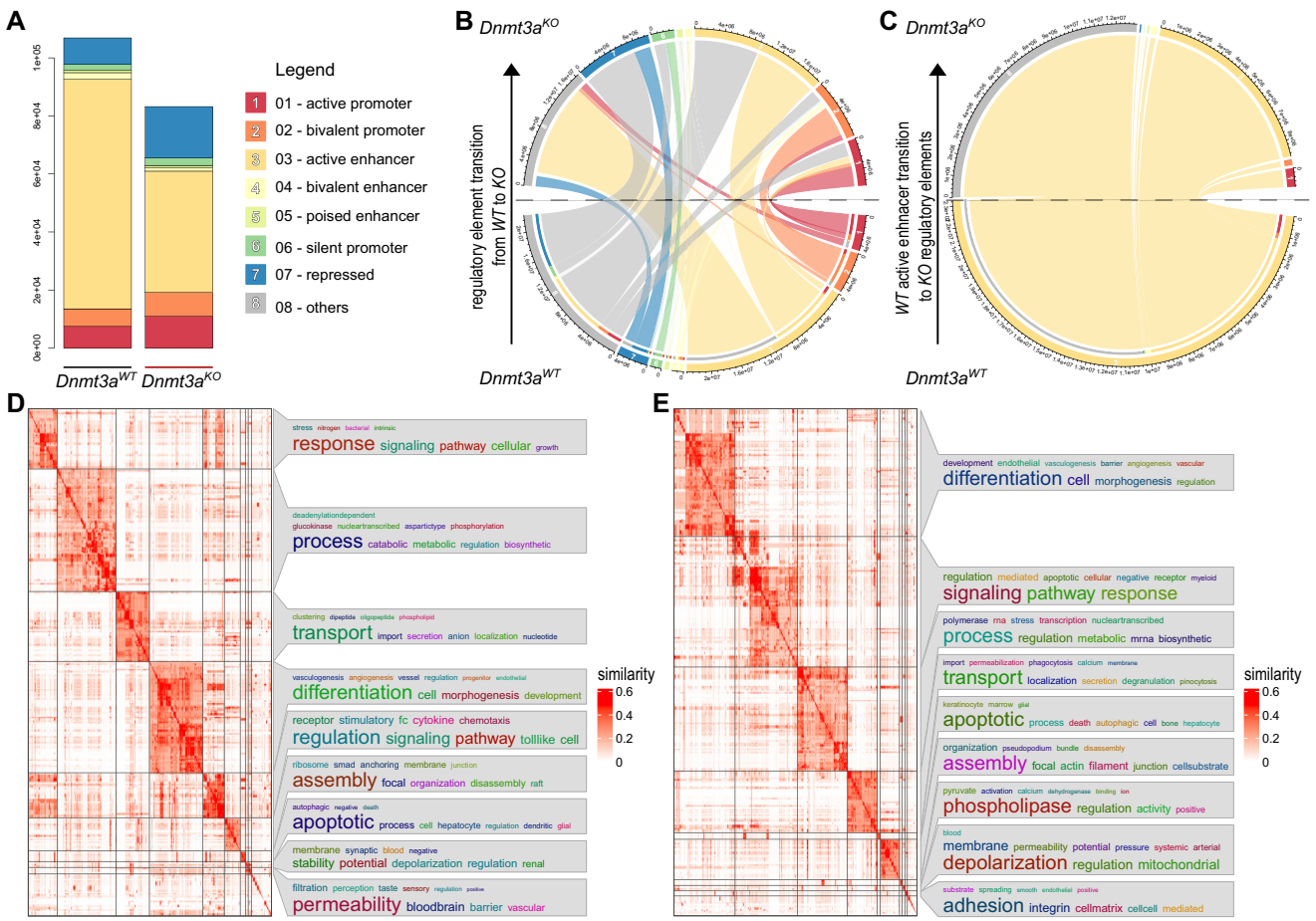

Figure 4. The absence of DNMT3A-dependent DNA methylation results in enhancer loss. (**A**) Bar plot showing the number of identified regulatory elements and silent chromatin in *Dnmt3a* WT and KO pulmonary ECs. (**B**) Circos plot showing the transition of all regulatory regions identified in *Dnmt3a* WT pulmonary ECs compared with *Dnmt3a* KO ECs. Regions are depicted in bp. (**C**) Focused circos plot of identified active enhancers in *Dnmt3a* WT pulmonary ECs (23,267,740 bp) and their change into other CRE categories in *Dnmt3a* KO ECs. This plot only focuses on active enhancers in WT ECs and does not include newly established active enhancers in KO ECs, which were gained due to conversions from non-assigned regions, among others, in WT ECs. Regions are depicted in bp. (**D**) Gene ontology analysis based on lost active enhancer regions in *Dnmt3a* WT compared to *Dnmt3a* KO ECs. GO terms were based on similarity, ranging from 0 to 0.8 (panel 3). The letter size represents the significance of the GO term (right). (**E**) Gene ontology analysis based on consistent active enhancer regions identified in both *Dnmt3a* WT and *Dnmt3a* KO ECs. GO terms were based on similarity, ranging from 0 to 0.8 (panel 3). The letter size represents the significance of the GO term (right).

transitioned into bivalent promoters, and 1,016,014 bp (21.57%) lost a defined CRE classification. Only minor fractions of WT active promoters transitioned into active enhancers (1.66% corresponding to 78,092 bp), poised enhancers (0.07% corresponding to 3,079 bp), and repressed states (0.14% corresponding to 6,805 bp). Overall, the genomic coverage of active promoters in KO ECs increased to 6,301,991 bp, due to the conversion of previously undefined chromatin ("others") (1,965,546 bp), active enhancers (863,324 bp), and bivalent promoters (564,516 bp) from WT ECs into active promoters in KO ECs (Fig. 4B and Supplementary Table S10).

Bivalent and silent promoter regions remained mostly stable in KO compared to WT ECs (Fig. 4B and Supplementary Table S10). From the bivalent promoters in WT (5,438,062 bp total genomic coverage), 78.54% (4,271,290 bp) were preserved in KO ECs, 10.38% (564,516 bp) transitioned from a bivalent promoter state in WT to an active promoter state in KO, and 8.87% (482,459 bp) lost a defined CRE classification in KO ECs. Due to the conversion from active promoters (799,567 bp), active enhancers (275,745 bp), bivalent enhancers (584,505 bp), and previously non-assigned CREs (1,648,272 bp) in WT ECs, the genomic coverage in KO ECs for bivalent promoters increased to 7,991,447 bp compared to 5,438,062 bp identified in WT ECs.

Similarly, silent promoters in WT (1,506,906 bp total genome coverage) were primarily retained in KO ECs (75.77% corresponding to 1,141,742 bp). Overall, 9.54% (143,830 bp) transitioned from a silent promoter state to a bivalent promoter state in KO ECs, and 11.49% (173,204 bp) were assigned as "others". The total genome coverage of silent promoters increased in KO compared to WT ECs largely due to the conversion from poised enhancers (102,404 bp), repressed regions (187,798 bp), and non-assigned regions (1,556,750 bp) in WT ECs to silent promoters in KO ECs (Fig. 4B and Supplementary Table S10).

A substantial proportion of CREs lost their classification upon *Dnmt3a* loss, as reflected in the "others" category in KO ECs. This effect was most pronounced for active enhancers (12,949,262 bp reassigned), bivalent enhancers (17.17% corresponding to 265,984 bp out of 1,548,815 bp total genome coverage of bivalent enhancers in WT ECs),

and repressed regions (35.34% corresponding to 1,465,917 bp out of 4,148,531 bp total genome coverage of repressed regions in WT ECs). However, out of the repressed regions, 55.56% (2,304,921 bp) remained repressed upon *Dnmt3a* KO (Fig. 4B and Supplementary Table S10). Taken together, the loss of *Dnmt3a* led to a reduction in active enhancers due to the transition into non-assigned chromatin states. Additionally, *Dnmt3a* deletion resulted in a gain of active promoters, largely through the conversion of undefined chromatin ("others") into functional CREs.

Enhancer loss in *Dnmt3a* KO ECs is not associated with specific biological functions

Next, we determined whether the loss of active enhancers in *Dnmt3a* KO ECs affected specific GO terms related to biological processes and explored the downstream consequences on gene expression. Region-based GO term analysis for lost enhancers in the *Dnmt3a* KO was enriched for biological processes related to signaling response, metabolic processes, differentiation, and cellular transport (Fig. 4D). Stable enhancers present in both the WT and *Dnmt3a* KO ECs were similarly enriched for differentiation, signaling response, metabolic processes, and cellular transport (Fig. 4E). The similarity in GO term enrichment between lost and stable active enhancers suggested a potential compensatory mechanism in which remaining enhancers may regulate genes previously controlled by lost enhancers.

To further explore the potential impact of DNA methylation changes on chromatin organization, we examined whether the identified DMRs upon *Dnmt3a* loss overlapped with known TF binding motifs. Specifically, motif analysis of distal hypomethylated DMRs upon *Dnmt3a* loss revealed a significant enrichment for TF binding sites associated with Fox family members (FOXO1, FOXO3, FOXA2, FOXA3, FOXF1, FOXH1, FOXP1), GATA factors (GATA1, GATA2, GATA3, GATA4, GATA6), homeobox TFs (HOXA1, HOXA2, HOXB4, DLX3, DLX5), and additional regulators (Supplementary Fig. S6). Moreover, we observed motif enrichment in both distal and local DMRs for COUP-TFII, EAR2, FOXA1, Smad2, Smad4, and Zfp281, among others (Supplementary Fig. S6). However, no enrichment was observed for CTCF (CCCTC-binding factor), YY1, or ZNF143, which are well known for their roles as architectural proteins and in mediating chromatin looping [52, 53]. This might suggest that DNA methylation loss in the endothelium affects more local chromatin remodeling processes rather than global chromatin architecture [54–56].

Discussion

The impact of DNA methylation on gene expression has been a subject of active research for several years. Here, we conducted an analysis of the pulmonary endothelial methylome over a longitudinal developmental timeline in mice. Our analyses revealed two key findings: first, significant changes in the methylome occur during the transition from an angiogenic to a quiescent state, and second, the stability of DNA methylation marks after the establishment of the quiescent state during aging. During this transition, we identified a subset of genes with correlated DNA methylation and gene expression, the majority of which were more highly methylated in the angiogenic state. Further research revealed DNMT3A as a DNA methyltransferase responsible for establishing DNA methylation in angiogenic ECs. The paradox of hypermethylation in actively transcribed genes and their increased expression is likely explained by the recognition of H3K36me3 by DNMTs [48, 57, 58]. Minor DNA methylation changes in EC^{mAdu} compared to EC^{aged} may be attributed to vascular reactivation caused by inflammation [59]. The resulting increase in gene expression, compared to ECs in a quiescent state, might impact the DNA methylation levels of these genes. However, this observation was not further investigated.

DNA hypomethylation upon loss of *Dnmt3a* changed the epigenetic landscape, leading to the loss of (i) chromatin accessibility and (ii) active enhancers in KO ECs. Counterintuitively, these epigenetic changes did not result in extensive gene deregulation, in line with the published literature [23, 60, 61]. This paradoxical observation may be explained by the complex interplay between multiple enhancer elements and their associated promoters, potentially compensating for each other's loss and maintaining consistent gene expression [62, 63]. Additionally, it is possible that many of the lost enhancers were originally linked to genes that are weakly expressed or transcriptionally silent in this context. However, without direct enhancer–promoter connectivity data, we cannot definitively determine whether the affected enhancers were functionally active or just poised for activation [64, 65]. This highlights the need for future studies incorporating chromatin conformation and enhancer perturbation approaches to dissect the functional consequences of enhancer loss. Despite this limitation, our findings underscore the complexity of enhancer regulation and suggest that enhancer loss alone is not necessarily sufficient to drive widespread gene expression changes. This raises the question of whether DNA methylation itself plays a role in stabilizing enhancer activity beyond its direct impact on transcriptional regulation. Recent research suggests that DNA methylation may stabilize the chromatin landscape at enhancer regions, preventing a shift toward a repressive state. In mouse embryonic stem cells, DNA hypomethylation was shown to cause loss of H3K27ac and gain of the repressive mark H3K27me3 at enhancers [66]. Additionally, bivalent enhancers with both H3K27ac and DNA methylation were shown to lose their activating histone mark when DNA methylation was removed [67], indicating that methylation plays a stabilizing role at these critical regulatory sites. However, our observed increase in repressive elements upon *Dnmt3a* loss appears counterintuitive to parts of the published literature, where the loss of *Dnmt3a* and DNA hypomethylation have been associated with reduced distribution of H3K27me3 [51, 68].

DNA methylation, especially at regulatory elements, has been generally considered to prohibit TF binding, leading to transcriptional downregulation. However, the loss of DNA methylation upon *Dnmt3a* deletion in ECs did not cause widespread gene deregulation but instead resulted in altered chromatin accessibility and enhancer remodeling. These findings suggest that the classical concept of DNA methylation as a mainly repressive mark may not fully apply to the endothelial epigenome. This raises an intriguing question: How does DNA methylation shape enhancer function and TF binding in the endothelium? In addition to its repressive role, DNA methylation may also positively influence transcription by re-

cruiting methylation-sensitive TFs. Intriguingly, gene ontology analysis of TFs that prefer methylated CpG sites within their motifs revealed associations with angiogenesis [15]. This finding aligns with the observed reduction in EC proliferation following the loss of DNA methylation [23], supporting the idea that methylation could be crucial for maintaining the proliferative potential of angiogenic ECs. In relation to our presented findings, we suggest that the role of DNA methylation in endothelial transcriptional control is more complex. Rather than acting as a primary determinant of transcription, it may serve as a fine-tuning mechanism, modulating TF binding affinity and enhancer responsiveness under specific conditions.

For example, the important endothelial TF KLF4 has been shown to preferentially bind to methylated CpG sites in regulatory elements, leading to chromatin remodeling and gene activation. In fact, the binding of KLF4 to methylated enhancers has been linked to phenotypically increased cell migration in glioblastoma cells, due to the direct activation of 116 genes [69]. This suggests that DNA methylation-mediated TF recruitment can, in certain contexts, drive gene activation rather than repression. However, in ECs, where *Dnmt3a* loss did not lead to widespread transcriptional changes, it is likely that KLF4 binding alone is not sufficient to induce gene activation. Instead, methylation-dependent TF binding may act as a priming mechanism, facilitating chromatin accessibility and enhancer activation in response to additional regulatory inputs [70]. These findings suggest a context-dependent role for DNA methylation in transcriptional regulation. While methylation-sensitive TFs such as KLF4 may promote transcription in some cell types, in ECs, DNA methylation may primarily function to stabilize enhancer states, ensuring regulatory element readiness rather than directly inducing gene expression. This aligns with our observation that enhancer loss in *Dnmt3a* KO ECs did not lead to transcriptional deregulation, likely due to enhancer redundancy and compensatory mechanisms that preserve gene expression stability.

Taken together, the findings of this study suggest that DNA methylation in ECs is not a primary determinant of gene expression but rather contributes to the fine-tuning of endothelial transcriptional programs. This model provides a more nuanced understanding of DNA methylation as a dynamic regulatory mark that modulates, rather than dictates, endothelial gene expression.

Acknowledgements

We would like to acknowledge the excellent technical support of Claudine Fricke (H.G.A. laboratory), Leon Blankenhorn (H.G.A. laboratory) as well as Marion Bähr (C.P. laboratory). We thank the Flow Cytometry Core Facility and the Central Animal Laboratory, German Cancer Research Center (DKFZ), for providing excellent services. We thank the High Throughput Sequencing unit of the Genomics and Proteomics Core Facility (DKFZ) for providing excellent sequencing and quality control analysis services. We thank the Light Microscopy Core Facility (DKFZ) for providing the instruments. The graphical abstract a schematic figures in this manuscript were created in BioRender. Augustin, H. (2025) https://BioRender.com/k83b042.

Author contributions: S.G., H.G.A., C.P., and K.S. conceived the study. S.G., D.W., J.H., N.B., and K.S. performed the experiments. S.G., Z.G., J.H., A.H.W., and K.B. analyzed the sequencing data. S.G. wrote the original draft of the manuscript. All authors reviewed and edited the manuscript. K.S., C.P., and H.G.A. supervised the study and acquired the funding.

Supplementary data

Supplementary data is available at NAR online.

Conflict of interest

None declared.

Funding

This work was supported by grants from the Deutsche Forschungsgemeinschaft (DFG) (Collaborative Research Center CRC1366 "Vascular Control of Organ Function" [project number 39404578 to K.S., C.P., and H.G.A]), the European Research Council Advanced Grant AngioMature [project 787181 to H.G.A.], the German Center for Lung Disease [to C.P.], and the German–Israeli Helmholtz International Research School Cancer-TRAX [HIRS-0003 to S.G.]. Funding to pay the Open Access publication charges for this article was provided by DKFZ Heidelberg.

Data availability

All raw sequencing data and annotated and filtered count matrices generated in this study are publicly available via GEO. WGBS data generated from FACS-sorted lung ECs from WT mice (mature adult and aged) are available under the following GEO accession number: GSE281950. RNA-seq data generated from FACS-sorted lung ECs from WT mice (mature adult and aged) are available under the following GEO accession number: GSE295387. RNA-seq, WGBS, ATAC-seq, and ACT-seq data generated from FACS-sorted lung ECs from both *Dnmt3a* KO and WT mice are available under the following GEO accession numbers: RNA-seq (GSE281342), WGBS (GSE281244), ATAC-seq (GSE281243), and ACT-seq (GSE281240). No original code is reported in this study. Further information and requests for resources should be directed to and will be fulfilled by the lead contact, Hellmut G. Augustin (augustin@angioscience.de).

References

1. Herbert SP, Stainier DYR. Molecular control of endothelial cell behaviour during blood vessel morphogenesis. *Nat Rev Mol Cell Biol* 2011;**12**:551–64. https://doi.org/10.1038/nrm3176
2. Trimm E, Red-Horse K. Vascular endothelial cell development and diversity. *Nat Rev Cardiol* 2023;**20**:197–210. https://doi.org/10.1038/s41569-022-00770-1
3. Ricard N, Bailly S, Guignabert C *et al.* The quiescent endothelium: signalling pathways regulating organ-specific endothelial normalcy. *Nat Rev Cardiol* 2021;**18**:565–80. https://doi.org/10.1038/s41569-021-00517-4
4. Schlereth K, Weichenhan D, Bauer T *et al.* The transcriptomic and epigenetic map of vascular quiescence in the continuous lung endothelium. *eLife* 2018;**7**:e34423. https://doi.org/10.7554/eLife.34423
5. Cedar H, Bergman Y. Linking DNA methylation and histone modification: patterns and paradigms. *Nat Rev Genet* 2009;**10**:295–304. https://doi.org/10.1038/nrg2540

6. Klemm SL, Shipony Z, Greenleaf WJ. Chromatin accessibility and the regulatory epigenome. *Nat Rev Genet* 2019;**20**:207–20. https://doi.org/10.1038/s41576-018-0089-8
7. Deaton AM, Bird A. CpG islands and the regulation of transcription. *Genes Dev* 2011;**25**:1010–22. https://doi.org/10.1101/gad.2037511
8. Herman JG, Lapidus RG, Issa JPJ *et al.* Inactivation of the CDKN2/pl6/MTS1 gene is frequently associated with aberrant DNA methylation in all common human cancers. *Cancer Res* 1995;**55**:4525–30.
9. Merlo A, Herman JG, Mao L *et al.* 5′ CpG island methylation is associated with transcriptional silencing of the tumour suppressor p16/CDKN2/MTS1 in human cancers. *Nat Med* 1995;**1**:686–92. https://doi.org/10.1038/nm0795-686
10. Parry A, Rulands S, Reik W. Active turnover of DNA methylation during cell fate decisions. *Nat Rev Genet* 2021;**22**:59–66. https://doi.org/10.1038/s41576-020-00287-8
11. Argelaguet R, Lohoff T, Li JG *et al.* Decoding gene regulation in the mouse embryo using single-cell multi-omics. bioRxiv, https://doi.org/10.1101/2022.06.15.496239, 15 November 2022, preprint: not peer reviewed.
12. Stadler MB, Murr R, Burger L *et al.* DNA-binding factors shape the mouse methylome at distal regulatory regions. *Nature* 2011;**480**:490–5. https://doi.org/10.1038/nature10716
13. Kress C, Thomassin H, Grange T. Active cytosine demethylation triggered by a nuclear receptor involves DNA strand breaks. *Proc Natl Acad Sci USA* 2006;**103**:11112–7. https://doi.org/10.1073/pnas.0601793103
14. Watt F, Molloy PL. Cytosine methylation prevents binding to DNA of a HeLa cell transcription factor required for optimal expression of the adenovirus major late promoter. *Genes Dev* 1988;**2**:1136–43. https://doi.org/10.1101/gad.2.9.1136
15. Yin Y, Morgunova E, Jolma A *et al.* Impact of cytosine methylation on DNA binding specificities of human transcription factors. *Science* 2017;**356**:eaaj2239. https://doi.org/10.1126/science.aaj2239
16. Boyes J, Bird A. DNA methylation inhibits transcription indirectly via a methyl-CpG binding protein. *Cell* 1991;**64**:1123–34. https://doi.org/10.1016/0092-8674(91)90267-3
17. Ng HH, Zhang Y, Hendrich B *et al.* MBD2 is a transcriptional repressor belonging to the MeCP1 histone deacetylase complex. *Nat Genet* 1999;**23**:58–61. https://doi.org/10.1038/12659
18. Sabbagh MF, Heng JS, Luo C *et al.* Transcriptional and epigenomic landscapes of CNS and non-CNS vascular endothelial cells. *eLife* 2018;**7**:e36187. https://doi.org/10.7554/eLife.36187
19. Hon GC, Rajagopal N, Shen Y *et al.* Epigenetic memory at embryonic enhancers identified in DNA methylation maps from adult mouse tissues. *Nat Genet* 2013;**45**:1198–206. https://doi.org/10.1038/ng.2746
20. Sharifi-Zarchi A, Gerovska D, Adachi K *et al.* DNA methylation regulates discrimination of enhancers from promoters through a H3K4me1–H3K4me3 seesaw mechanism. *BMC Genomics* 2017;**18**:964. https://doi.org/10.1186/s12864-017-4353-7
21. Okano M, Bell DW, Haber DA *et al.* DNA methyltransferases Dnmt3a and Dnmt3b are essential for *de novo* methylation and mammalian development. *Cell* 1999;**99**:247–57. https://doi.org/10.1016/S0092-8674(00)81656-6
22. Li E, Bestor TH, Jaenisch R. Targeted mutation of the DNA methyltransferase gene results in embryonic lethality. *Cell* 1992;**69**:915–26. https://doi.org/10.1016/0092-8674(92)90611-F
23. Gehrs S, Jakab M, Gutjahr E *et al.* The spatial zonation of the murine placental vasculature is specified by epigenetic mechanisms. *Dev Cell* 2025;**60**:1467–82. https://doi.org/10.1016/j.devcel.2024.12.037
24. Heinz S, Benner C, Spann N *et al.* Simple combinations of lineage-determining transcription factors prime *cis*-regulatory elements required for macrophage and B cell identities. *Mol Cell* 2010;**38**:576–89. https://doi.org/10.1016/j.molcel.2010.05.004
25. Bray NL, Pimentel H, Melsted P *et al.* Near-optimal probabilistic RNA-seq quantification. *Nat Biotechnol* 2016;**34**:525–7. https://doi.org/10.1038/nbt.3519
26. McGarvey KM, Goldfarb T, Cox E *et al.* Mouse genome annotation by the RefSeq project. *Mamm Genome* 2015;**26**:379–90. https://doi.org/10.1007/s00335-015-9585-8
27. Love MI, Huber W, Anders S. Moderated estimation of fold change and dispersion for RNA-seq data with DESeq2. *Genome Biol* 2014;**15**:550. https://doi.org/10.1186/s13059-014-0550-8
28. Gu Z, Schlesner M, Hübschmann D. cola: an R/Bioconductor package for consensus partitioning through a general framework. *Nucleic Acids Res* 2021;**49**:e15. https://doi.org/10.1093/nar/gkaa1146
29. Yu G, Wang LG, Han Y *et al.* clusterProfiler: an R package for comparing biological themes among gene clusters. *OMICS* 2012;**16**:284–7. https://doi.org/10.1089/omi.2011.0118
30. Gu Z, Hübschmann D. simplifyEnrichment: a Bioconductor package for clustering and visualizing functional enrichment results. *Genomics Proteomics Bioinformatics* 2023;**21**:190–202. https://doi.org/10.1016/j.gpb.2022.04.008
31. Gu Z, Eils R, Schlesner M. Complex heatmaps reveal patterns and correlations in multidimensional genomic data. *Bioinformatics* 2016;**32**:2847–9. https://doi.org/10.1093/bioinformatics/btw313
32. Gu Z, Eils R, Schlesner M *et al.* EnrichedHeatmap: an R/Bioconductor package for comprehensive visualization of genomic signal associations. *BMC Genomics* 2018;**19**:234. https://doi.org/10.1186/s12864-018-4625-x
33. Lee J, Christoforo G, Foo C *et al.* kundajelab/atac_dnase_pipelines: 0.3.0. Zenodo. 2016. https://doi.org/10.5281/ZENODO.156534
34. Krueger F. *Trim Galore! version 0.4.4*. Cambridge, United Kingdom: Bioinformatics Group, Babraham Institute. 2017. http://www.bioinformatics.babraham.ac.uk/projects/trim_galore
35. Martin M. Cutadapt removes adapter sequences from high-throughput sequencing reads. *EMBnet J* 2011;**17**:10–2. https://doi.org/10.14806/ej.17.1.200
36. Langmead B, Salzberg SL. Fast gapped-read alignment with Bowtie 2. *Nat Methods* 2012;**9**:357–9. https://doi.org/10.1038/nmeth.1923
37. Li H, Handsaker B, Wysoker A *et al.* The Sequence Alignment/Map format and SAMtools. *Bioinformatics* 2009;**25**:2078–9. https://doi.org/10.1093/bioinformatics/btp352
38. Adey A, Morrison HG, Asan Xun X *et al.* Rapid, low-input, low-bias construction of shotgun fragment libraries by high-density *in vitro* transposition. *Genome Biol* 2010;**11**:R119. https://doi.org/10.1186/gb-2010-11-12-r119
39. Buenrostro JD, Giresi PG, Zaba LC *et al.* Transposition of native chromatin for fast and sensitive epigenomic profiling of open chromatin, DNA-binding proteins and nucleosome position. *Nat Methods* 2013;**10**:1213–8. https://doi.org/10.1038/nmeth.2688
40. Ramírez F, Ryan DP, Grüning B *et al.* deepTools2: a next generation web server for deep-sequencing data analysis. *Nucleic Acids Res* 2016;**44**:W160–5. https://doi.org/10.1093/nar/gkw257
41. Amstutz P, Crusoe MR, Tijanić N *et al.* Common Workflow Language, v1.0. Figshare. 2016. https://doi.org/10.6084/M9.FIGSHARE.3115156
42. Breuer K, Assenov Y, Lutsik P *et al.* Highly portable workflow suite based on the Common Workflow Language for processing of data generated by ChIP-seq, ChIPmentation, Cut&Run, and ACT-seq. Zenodo. 2020. https://doi.org/10.5281/ZENODO.3970149
43. Zhang Y, Liu T, Meyer CA *et al.* Model-based analysis of ChIP-Seq (MACS). *Genome Biol* 2008;**9**:R137. https://doi.org/10.1186/gb-2008-9-9-r137
44. Mohn F, Weber M, Rebhan M *et al.* Lineage-specific Polycomb targets and *de novo* DNA methylation define restriction and potential of neuronal progenitors. *Mol Cell* 2008;**30**:755–66. https://doi.org/10.1016/j.molcel.2008.05.007

45. Greenberg MVC, Bourc'his D. The diverse roles of DNA methylation in mammalian development and disease. *Nat Rev Mol Cell Biol* 2019;**20**:590–607. https://doi.org/10.1038/s41580-019-0159-6
46. Larsen F, Gundersen G, Lopez R *et al.* CpG islands as gene markers in the human genome. *Genomics* 1992;**13**:1095–107. https://doi.org/10.1016/0888-7543(92)90024-M
47. Irizarry RA, Ladd-Acosta C, Wen B *et al.* The human colon cancer methylome shows similar hypo- and hypermethylation at conserved tissue-specific CpG island shores. *Nat Genet* 2009;**41**:178–86. https://doi.org/10.1038/ng.298
48. Jones PA. Functions of DNA methylation: islands, start sites, gene bodies and beyond. *Nat Rev Genet* 2012;**13**:484–92. https://doi.org/10.1038/nrg3230
49. Mao SQ, Cuesta SM, Tannahill D *et al.* Genome-wide DNA methylation signatures are determined by DNMT3A/B sequence preferences. *Biochemistry* 2020;**59**:2541–50. https://doi.org/10.1021/acs.biochem.0c00339
50. Manzo M, Wirz J, Ambrosi C *et al.* Isoform-specific localization of DNMT3A regulates DNA methylation fidelity at bivalent CpG islands. *EMBO J* 2017;**36**:3421–34. https://doi.org/10.15252/embj.201797038
51. Gu T, Lin X, Cullen SM *et al.* DNMT3A and TET1 cooperate to regulate promoter epigenetic landscapes in mouse embryonic stem cells. *Genome Biol* 2018;**19**:88. https://doi.org/10.1186/s13059-018-1464-7
52. Sun X, Zhang J, Cao C. CTCF and its partners: shaper of 3D genome during development. *Genes* 2022;**13**:1383. https://doi.org/10.3390/genes13081383
53. Zhang M, Huang H, Li J *et al.* ZNF143 deletion alters enhancer/promoter looping and CTCF/cohesin geometry. *Cell Rep* 2024;**43**:113663. https://doi.org/10.1016/j.celrep.2023.113663
54. Lalmansingh AS, Karmakar S, Jin Y *et al.* Multiple modes of chromatin remodeling by Forkhead box proteins. *Biochim Biophys Acta* 2012;**1819**:707–15. https://doi.org/10.1016/j.bbagrm.2012.02.018
55. Ross S, Cheung E, Petrakis TG *et al.* Smads orchestrate specific histone modifications and chromatin remodeling to activate transcription. *EMBO J* 2006;**25**:4490–502. https://doi.org/10.1038/sj.emboj.7601332
56. Paul R, Peraldi R, Kmita M. The pioneering function of the hox transcription factors. *Semin Cell Dev Biol* 2024;**152–153**:85–92. https://doi.org/10.1016/j.semcdb.2022.11.013
57. Hahn MA, Wu X, Li AX *et al.* Relationship between gene body DNA methylation and intragenic H3K9me3 and H3K36me3 chromatin marks. *PLoS One* 2011;**6**:e18844. https://doi.org/10.1371/journal.pone.0018844
58. Dhayalan A, Rajavelu A, Rathert P *et al.* The Dnmt3a PWWP domain reads histone 3 lysine 36 trimethylation and guides DNA methylation. *J Biol Chem* 2010;**285**:26114–20. https://doi.org/10.1074/jbc.M109.089433
59. Haines DC, Chattopadhyay S, Ward JM. Pathology of aging B6;129 mice. *Toxicol Pathol* 2001;**29**:653–61. https://doi.org/10.1080/019262301753385988
60. Li J, Pinto-Duarte A, Zander M *et al.* Dnmt3a knockout in excitatory neurons impairs postnatal synapse maturation and increases the repressive histone modification H3K27me3. *eLife* 2022;**11**:e66909. https://doi.org/10.7554/eLife.66909
61. Andrews S, Krueger C, Mellado-Lopez M *et al.* Mechanisms and function of *de novo* DNA methylation in placental development reveals an essential role for DNMT3B. *Nat Commun* 2023;**14**:371. https://doi.org/10.1038/s41467-023-36019-9
62. Long HK, Prescott SL, Wysocka J. Ever-changing landscapes: transcriptional enhancers in development and evolution. *Cell* 2016;**167**:1170–87. https://doi.org/10.1016/j.cell.2016.09.018
63. Osterwalder M, Barozzi I, Tissiéres V *et al.* Enhancer redundancy provides phenotypic robustness in mammalian development. *Nature* 2018;**554**:239–43. https://doi.org/10.1038/nature25461
64. Schoenfelder S, Fraser P. Long-range enhancer–promoter contacts in gene expression control. *Nat Rev Genet* 2019;**20**:437–55. https://doi.org/10.1038/s41576-019-0128-0
65. Mumbach MR, Satpathy AT, Boyle EA *et al.* Enhancer connectome in primary human cells identifies target genes of disease-associated DNA elements. *Nat Genet* 2017;**49**:1602–12. https://doi.org/10.1038/ng.3963
66. King AD, Huang K, Rubbi L *et al.* Reversible regulation of promoter and enhancer histone landscape by DNA methylation in mouse embryonic stem cells. *Cell Rep* 2016;**17**:289–302. https://doi.org/10.1016/j.celrep.2016.08.083
67. Charlet J, Duymich CE, Lay FD *et al.* Bivalent regions of cytosine methylation and H3K27 acetylation suggest an active role for DNA methylation at enhancers. *Mol Cell* 2016;**62**:422–31. https://doi.org/10.1016/j.molcel.2016.03.033
68. Reddington JP, Perricone SM, Nestor CE *et al.* Redistribution of H3K27me3 upon DNA hypomethylation results in de-repression of Polycomb target genes. *Genome Biol* 2013;**14**:R25. https://doi.org/10.1186/gb-2013-14-3-r25
69. Wan J, Su Y, Song Q *et al.* Methylated *cis*-regulatory elements mediate KLF4-dependent gene transactivation and cell migration. *eLife* 2017;**6**:e20068. https://doi.org/10.7554/eLife.20068
70. Moonen J-R, Chappell J, Shi M *et al.* KLF4 recruits SWI/SNF to increase chromatin accessibility and reprogram the endothelial enhancer landscape under laminar shear stress. *Nat Commun* 2022;**13**:4941. https://doi.org/10.1038/s41467-022-32566-9

Received: November 21, 2024. **Revised:** March 28, 2025. **Editorial Decision:** April 26, 2025. **Accepted:** May 15, 2025